



Geometry and surface characteristics of H13 hot-work tool steel manufactured using laser-directed energy deposition

Owen Craig¹ · Alexandre Bois-Brochu² · Kevin Plucknett¹

Received: 3 February 2021 / Accepted: 20 May 2021 / Published online: 23 June 2021
© The Author(s), under exclusive licence to Springer-Verlag London Ltd., part of Springer Nature 2021

Abstract

This research focuses on specimen geometry and the associated surface roughness of H13 hot-work tool steel, processed using laser-directed energy deposition additive manufacturing, and varying both the powder feed rate and the laser scanning speed. Under the examined conditions, the test sample measurements of length and width did not vary, but the sample heights were significantly affected by the scanning speed. An increase in scan speed resulted in ‘underbuilding’, while a decrease resulted in ‘overbuilding’, as might be anticipated. The top surface roughness of the samples was found to be greater than the side surface roughness, due to the capture of extra powder particles. For the single-track and multitrack clad samples, the surface roughness was increased when decreasing the scan speed. The addition of a draft angle, when producing 3-D components, was shown to reduce the side surface roughness. Using a finer layer thickness results in overbuilding the target height, while a coarser layer thickness results in underbuilding. Finally, the surface roughness exhibited no clear trend when the layer thickness was changed.

Keywords Additive manufacturing · Directed energy deposition · Surface roughness · Tool steel · Confocal laser scanning microscopy

1 Introduction

AISI H13 is classified as a chromium-containing, hot-work tool steel for applications which require high wear resistance and toughness, with the ‘H’ designating it for use at elevated temperatures [1]. To achieve high hardness, it is heavily alloyed to produce carbides during subsequent heat treatment cycles. Common applications for H13 tool steel include dies for hot-forging, casting, and other hot-forming processes [1–3]. Due to the intrinsic application areas for these materials, combined with the probability of thermal cycling in use, the tooling may become sufficiently worn or damaged such that it must be either replaced or (preferably) repaired [1, 4, 5].

Additive manufacturing (AM) technologies typically build components layer by layer, and two moderately common approaches are based upon laser heating, to directly consolidate

the material during fabrication [6]; these are laser powder bed fusion (PBF) and laser-directed energy deposition (DED). In particular, DED uses a focused heat source, which can be either a laser or alternate energy source (*i.e.*, electron beam and electric arc) to generate a molten pool on the surface of the substrate, where fresh material is then deposited [6–9]. This technique lends itself especially well to component repair or cladding, for example with a different composition, as material can be deposited in specific locations for the repair of existing parts. It should also be stressed that freeform fabrication of components is possible with DED. The feedstock material can be either blown powder or, alternately, a continuous fed wire. A further benefit with laser DED is the ability to deposit a different material from the substrate, for example one with higher wear or corrosion resistance [10]. However, a currently limiting factor for laser DED, as well as other nonlaser-based DED approaches, is a relatively low surface finish, which invariably requires final machining [6, 11].

Since the locally deposited material is being fully melted in laser DED, nominally the same material composition can be deposited, and may ultimately be expected to behave similarly to a wrought equivalent during any subsequent heat treatment process. The final surface finish of laser-processed DED parts is an important factor to consider. If repair or net-shape parts

✉ Kevin Plucknett
kevin.plucknett@dal.ca

¹ Mechanical Engineering Department, Dalhousie University, Halifax, Nova Scotia B3J 1Z1, Canada

² Centre de Métallurgie du Québec (CMQ), Trois-Rivières, Québec G9A 5E1, Canada

are to be successfully implemented, the process parameters need to be optimized for the specific alloy and powder; this is a general challenge for such AM processes. By reducing the as-printed surface roughness, the need for postprocessing will also be reduced. Currently, DED has a lower quality exterior finish when compared to PBF, invariably creating a noticeable waviness to the surface [12]. This is due to the finer layer thickness in PBF, arising from the smaller ‘ideal’ particle sizes used. However, achieving an optimal surface finish does not guarantee simultaneously optimized mechanical properties. DED typically has higher deposition rates than PBF technologies [6], but the surface roughness suffers due to the particle size limitations previously noted; for comparison, the ideal mean particle size with PBF is $\approx 35 \mu\text{m}$ [13], whereas for DED it ranges from 50 to 150 μm [14].

A few reports have investigated the influence of changing the layer thickness on the deposited layer [15, 16], but have not studied the effects in terms of final surface roughness. There has also been research into the impact of build orientation [17], because of the anisotropic character of additive manufacturing. Studies into the roughness of sloped surfaces deposited through DED are limited [18], with comparable PBF-based research being more common in the open literature [19, 20]. Furthermore, research on AM metal surface finish has mainly been conducted on titanium [21–26] or stainless steel [18, 19, 27–31], and hence there is a need to extend this assessment to other materials.

The surface roughness can be expressed using a linear measurement, typically referred to as ‘ R_a ’; this is the difference in height compared to an arithmetical mean height along a linear direction for a fixed distance [32, 33]. Alternately, surface roughness can also be presented in a different ‘areal’ form, ‘ S_a ’, which expresses the difference in height compared to an arithmetical mean over a fixed area [33]. With this in mind, the purpose of the present research is to study the influence that changing specific laser DED process parameters (*i.e.*, scanning speed and feed rate) has on the geometry and surface finish of deposited H13 hot-work tool steel.

2 Experimental procedure

2.1 Raw materials

In this investigation, a prealloyed H13 gas atomized powder was purchased from TLS Technik (Bitterfeld-Wolfen, Germany); the powder was specified at the time of order to have a nominal size within the range of 50–100 μm . The particle size distribution (PSD) of the ‘as-received’ powders was then determined using particle size analysis (model Mastersizer 3000, Malvern Instruments, Malvern, UK); three measurements were undertaken on different samples from the supplied batch to assess ‘inbatch’ variability. The H13

powder surface morphology and size distribution were then examined using field emission scanning electron microscopy (FE-SEM; model S4700, Hitachi High Technologies, Tokyo, Japan). For imaging purposes, the FE-SEM was usually operated with an accelerating voltage, V_{acc} , of 5 kV and a beam current, I_c , of 20 μA . Samples of the ‘as-received’ powder were also cold mounted in epoxy resin, which was then polished to a 1 μm surface finish, to assess their cross-sectional structure via optical microscopy (OM; model BX-51, Olympus Corp., Tokyo, Japan) and FE-SEM. In particular, this process was conducted to detect any evidence of internal porosity and, if present, to see if it has any impact on the surface finish or final component density. For the subsequent laser DED processing, the powder was sieved from $-45/+135$ mesh to remove any ‘fines’ and ensure consistent flow characteristics in the powder feeder.

The substrate material used for all deposition studies were wrought, annealed H13 plates, purchased from Hudson Tool Steel Corporation (Rockford, IL, USA), with dimensions 165.1 mm \times 152.4 mm \times 15.875 mm. Before any DED printing was conducted the substrate was sandblasted ($-20/+60$ grit). The composition of the ‘as-received’ H13 powder and substrate was determined with inductively coupled plasma optical emission spectrometry (ICP-OES; model Vista-PRO, Varian Inc., CA, USA), with an internal calibration standard (scandium). The carbon content was determined using a carbon-sulfur combustion analyzer (model CS2000, Eltra GmbH, Haan, Germany) following the ASTM Standard E1941-10: *Standard Test Method for Determination of Carbon in Refractory and Reactive Metals and Their Alloys by Combustion Analysis*. The ICP-OES and carbon analyses were conducted three times on both the powder and substrate to obtain an average value in each case, which is provided in Table 1, along with the associated American Iron and Steel Institute (AISI) specifications for this steel grade.

The apparent density of the as-received powder was determined following ASTM standard B703-17: *Standard Test Method for Apparent Density of Metal Powders and Related Compounds Using the Arnold Meter*. Similarly, the flow characteristics were determined using a Hall Flowmeter, following ASTM standard B213-20: *Standard Test Methods for Flow Rate of Metal Powders Using the Hall Flowmeter Funnel*.

2.2 Laser DED system parameters

The laser DED equipment used in the present investigation was a 3-axis LENSTM 450XL system (Optomec, Albuquerque, NM, USA), using a 400 W continuous Nd:YAG laser, and with high purity Ar used as both the powder carrier gas (5 L/min flow rate) and the protective shield gas (25–30 L/min flow rate), to minimize oxidation during deposition. The system is initially under nominally atmospheric conditions in the build chamber, at ambient temperature, with

Table 1 Chemical compositions of the ‘as-received’ H13 powder (prior to DED use), wrought H13 substrate and the post-DED ‘recovered’ powder. AISI standard specifications are provided vs. measured values (note that Fe comprises the balance in each case)

Designation	Composition (wt.%)					
	C	Si	Mn	Cr	Mo	V
AISI H13	0.32–0.45	0.8–1.2	0.2–0.5	4.75–5.5	1.1–1.75	0.8–1.2
As-received powder	0.372	1.02	0.42	5.74	1.46	1.05
Substrate	0.39	0.63	0.30	4.73	1.37	0.80
Recovered powder	0.36	0.74	0.42	5.57	1.44	1.12

a 15-min purge of Ar then conducted. The Ar content within the chamber then increases continuously during laser deposition. The system operating parameters employed for the single-track clad, multitrack clad, and rectangular samples are listed in Table 2; sample geometries are discussed in greater detail in Section 2.3: *Sample Test geometries*.

2.3 Sample test geometries

The single-track clad, multitrack clad, and rectangular samples were deposited using a variety of laser DED printing parameters, resulting in 20 samples for each complete parameter set; Fig. 1 presents a schematic representation of these various printed geometries. Both the single-track and multitrack clad samples have an overall length of 25 mm, and are all one deposition layer thick. The multitrack cladding samples each consisted of six aligned and slightly overlapping tracks; in this instance the applied hatch spacing was 0.381 mm. The nominal dimensions of the rectangular samples were 5 mm × 25 mm × 10 mm. The identification schemes used for the single-track clad, multitrack clad, and rectangular sample are provided in Table 3.

Two further sample geometries were also assessed, in order to investigate their impact upon the final surface finish and deposition height error. These were nominally cube-based samples, with various draft angles (α) ranging from 10 to 85°, with the dashed line indicating the ‘draft face’ from which the surface roughness measurements were taken (Fig.

Table 2 The DED system operating parameters used for the present study

Parameter	Value	Units
Laser power	400	W
Scan speed	400–700	mm/minute
Feed rate	5.5–7.5	g/minute
Hatch spacing	0.381	mm
Layer thickness	0.251	mm
Spot size	600	μm
Nozzle stand off	9.525	mm
Hatch orientation	0°, 45°, 90°, 135°	degrees

1(b)), and simple cubic ‘ideal layer thickness’ samples, with nominal deposition layer thicknesses ranging from 0.2032 to 0.3302 mm, and with a final targeted build height of 10 mm. Regression statistical analysis (Minitab®, State College, PA, USA) was used, with a confidence interval of 0.05, to see if changes to the selected deposition parameters were significant; this means a *P* value less than or equal to 0.05 is viewed as being significant. The ANOVA software feature was used to generate a significance ‘main effects plot’ and related contour plot. The main effects plots show if parameters have similar impacts on the measured values. For each feed and speed value, the software creates a mean value (the points shown on each plot). If the points are connected by horizontal lines, then each parameter has effectively the same impact. However, if the line is not horizontal, then there is different impact for each parameter. A steeper slope then indicates a greater main effect. The dotted line presented on each ‘main effects’ graph is the overall mean. An ‘*R*-squared’ (*R*-sq) linear regression approach was used to predict if there is a trend in the data. The *R*-sq value (or coefficient of determination) represents the percentage of variance in the dependent variable which can be explained by the independent variable [34].

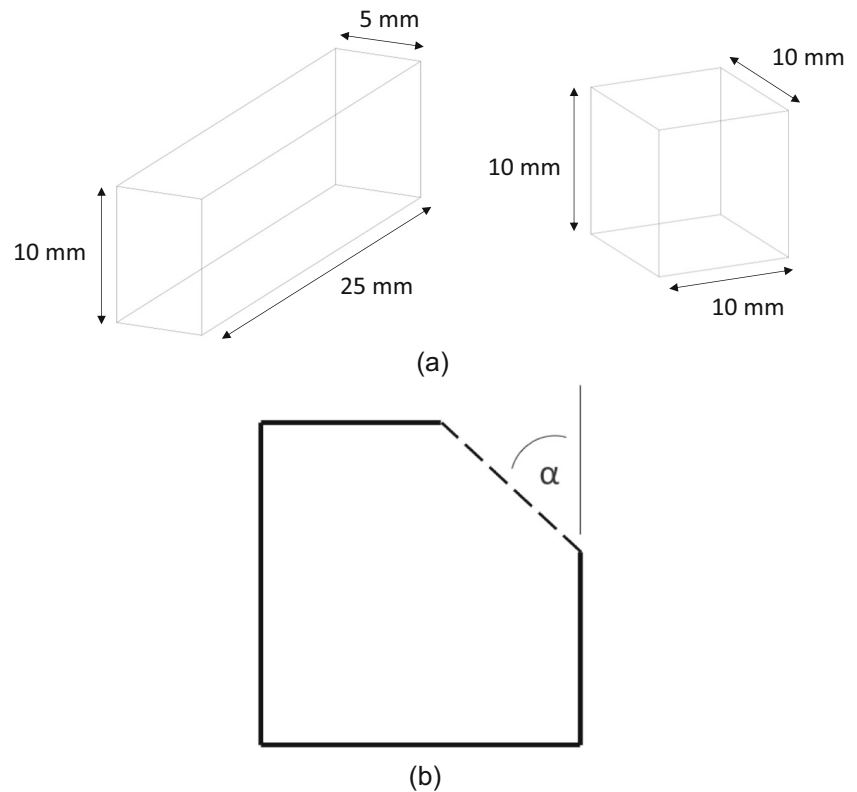
2.4 Sample characterisation

The initial dimensional accuracy was measured for each of the widths, lengths, and heights of the rectangular samples, together with the ideal layer thickness samples, with four measurements undertaken in each case to obtain an average dimensional value. Further dimensional analyses, including

Table 3 Sample identification for single-track clad, multitrack clad, and rectangular samples

Sample ID	Feed rate (g/min)					
	7.5	7	6.5	6	5.5	
Scan speed (mm/min)	700	A1	B1	C1	D1	E1
	600	A2	B2	C2	D2	E2
	500	A3	B3	C3	D3	E3
	400	A4	B4	C4	D4	E4

Fig. 1 **a** Schematic representations of the rectangle and ‘ideal layer thickness’ sample geometries that were examined. **b** Schematic representation of the draft angle (α) sample geometry with the dashed line indicating the draft face



measurement of the cladding surface roughness values, were conducted using a confocal laser scanning microscope (CLSM; model VK-X1100, Keyence Corp., Osaka, Japan). Data was analyzed on the CLSM using the Keyence *Multifile Analyzer* software. All samples are measured in the ‘as-printed’ condition, without further treatments (*e.g.*, annealing and tempering). For the single-track and multitrack cladding samples, four width measurements were taken with the CLSM, using a 20 \times magnification objective lens (with a theoretical resolution of 535.7 nm), to obtain an average for each single-track/multitrack width, which was then assessed as a function of the DED process parameters. The cross-sectional profiles of the single clad tracks were also evaluated using the CLSM, again using the 20 \times magnification objective lens, with four measurements also made for each sample to determine an average value.

In terms of the as-printed surface finish, a variety of roughness parameters were evaluated using the CLSM. Surface roughness (S_a) was recorded using the *Multifile Analyzer* software. Measurements were taken using a 20 \times magnification objective lens, as before. Surface analysis for the rectangles and ideal layer thickness samples were taken in the build height direction (Z-direction). The side plane was normalized for all measurements. The top surface roughness was measured in the X–Y plane with no normalization. In each case, five stitched images for the side and top surfaces were recorded for each of the mean values determined from the surface analysis. The draft samples were fixed in a mount allowing

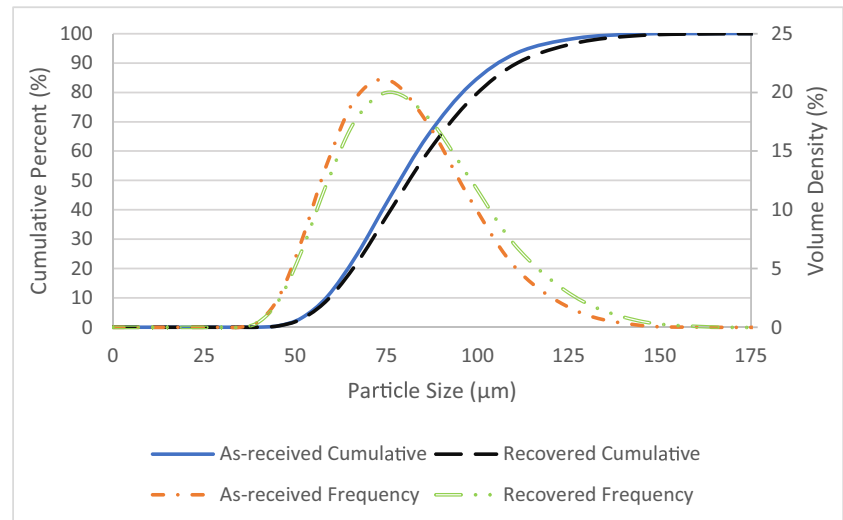
them to be rotated, to make the ‘draft face’ normal to the CLSM beam axis, and then the angle of the plane was finally finely adjusted (normalized) using the *Multifile Analyzer* software, with five stitched images used for further analysis, as before. For the single-track clad surface analysis, a single image was captured. The multitrack clad samples used between 4 and 5 stitched images, which were stitched ‘transversely’ along the scanning direction. None of the single- or multitrack clad samples required normalization due to the parallel faces of the substrate plates relative to the CLSM laser beam. Analysis areas were selected that had the least amount of attached, ‘satellite’ particles on the surface. For all samples, three data points were taken to get a mean value and associated standard deviation. No filtering was applied to the analyzed surfaces. Finally, to identify any surface porosity on the clads, FE-SEM was used, again operating with a V_{acc} of 5 kV and an I_e of 20 μ A.

3 Results and discussion

3.1 Feedstock powder characterisation

Figure 2 demonstrates a representative particle size distribution (PSD) for the as-received powder. From the overall PSD information, the mean starting particle size has values of: $D_{10} = 58.3 \mu\text{m}$, $D_{50} = 78.7 \mu\text{m}$, and $D_{90} = 107.0 \mu\text{m}$. Figure 3(a) shows a representative FE-SEM image of the as-received

Fig. 2 Representative examples of the particle size distributions for both the as-received and recovered H13 powder



powder, highlighting the overall particle morphology. It is apparent that the ‘as-supplied’, gas-atomized H13 powder has a generally spherical morphology, with some isolated

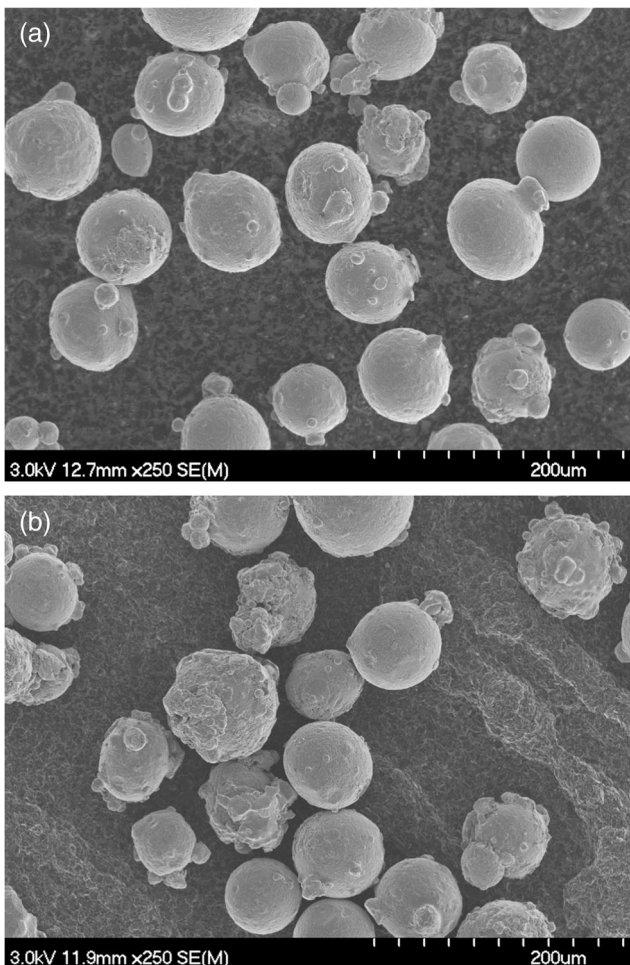


Fig. 3 **a** Typical example of the as-received H13 powder morphology viewed using FE-SEM. **b** Used and recovered H13 powder morphology examined using FE-SEM

satellite particles. In addition, cross-sectional examination (not shown) of the powder revealed it has minimal internal porosity. The as-received H13 powder had an apparent density of 4.260 g/cm^3 , following the ASTM standard B703-17. Using a Hall Flowmeter (ASTM standard B213-20), the flow rate of the virgin powder was 15.13 s/50 g . After laser deposition, the used (recovered) powder had a slightly reduced flow rate of 16.73 s/50 g , resulting in an increase of 10.45%. Figure 3(b) shows that the used powder, after running through the laser DED system, contains more satellites, but some particles still remain without any satellites. The extra surface satellites can lead to greater particle ‘interlocking’, decreasing the flowability of the powder. Interlocking may lead to entrapped gas from the local atmosphere during DED. A further issue with interlocking, is that it may clog the powder feeder/nozzle head, through the possibility of powder particles jamming within the nozzle head and/or powder feeding tube, however this is difficult to fully assess [35]. Kong and colleagues noted that with a smaller PSD, the deposition process ‘pulsed’ [36], due to the powder particles compacting within the nozzle. When the carrier gas pressure build-up was sufficient, it would unplug the nozzle and the process would repeat itself. The observations relating to morphology changes are promising for reuse of the powder. However, a powder flow test should still be conducted, in order to adjust the system parameters (if needed), thus ensuring the system powder feed rates remain consistent.

3.2 Single-track cladding geometry effects

A clear trend can be seen in terms of the effects of scanning speed, with faster speeds resulting in decreased single-track clad widths, as shown in Fig. 4(a). In this instance the widths, measured via CLSM, range from $585.05 \mu\text{m} \pm 9.43$ to $674.93 \mu\text{m} \pm 15.54$. The slower scanning speeds result in a wider track because there is higher energy input per unit

volume of material, which creates a larger melt pool [23]. The R -sq for the single-track clad widths is 82.14%. A reduction in the R -sq value in this instance could be attributed to noisy and high variance in the data set [34]. The P values obtained for the scanning speed and feed rate are 0.0 and 0.63, respectively (Table 4). Higher scanning speeds cause a reduction in the melt pool size, which consequently results in less consolidated material in each deposited track [21]. In addition, the increased feed rate means more particles are interacting with the laser beam, which in turn creates a smaller melt pool [24]. The likely reason that the scanning speed is a significant parameter is because it will determine how long powder particles can interact with both the laser beam and melt pool. Intuitively, a slower speed will result in a greater energy input, allowing for longer particle interaction with the laser and melt pool, consolidating more powder, and leading to wider tracks and larger cross-sections [29]. In terms of the overall influence of the examined process parameters (Fig. 4(b)), the powder feed rates do not have a significant impact on the track width. Conversely, the impact of the scanning speed is significant in terms of the measured track widths. Looking at the cross-sectional profiles of the single-track clads, again determined using the CLSM, the slower scan speeds resulted in the overall deposition of larger clads. The cross-sectional areas ranged from $19.5 \times 10^3 (\pm 3.7 \times 10^3) \mu\text{m}^2$ to $63.6 \times 10^3 (\pm 2.9 \times 10^3) \mu\text{m}^2$, with the highest feed rate resulting in the largest cross-sectional area (Fig. 4(c, d)). Conversely, the fastest scanning speed and lower feed rates resulted in the smallest cross-sectional areas.

It is apparent that the lowest and highest examined scanning speeds, namely 400 mm/min and 700 mm/min, have the greatest influence on the amount of material consolidated (*i.e.*, cross-sectional area). The cross-sectional area R -sq = 19.82%, with associated P values of 0.169 and 0.162 for the scanning speed and powder feed rate, respectively. It is clear there is no trend in the regression, but looking at the main effects plot, the magnitude of change in the feed rates is lower, when compared to the change in the scanning speeds from 400 mm/min to 700 mm/min.

Table 4 The system parameter significance (determined using ANOVA in Minitab®) on the widths of the single-track and multitrack clads, the rectangular samples, and the single-track clad cross-sectional areas (CSA)

Sample	R -sq (%)	Scanning speed P value	Feed rate P value
Single-track clad	82.14	0.0	0.63
Multitrack clad	37.23	0.088	0.018
Rectangle	90.68	0.0	0.062
CSA	19.82	0.169	0.162

Increasing the scanning speed results in a decrease of the clad height for the single-track clads, as shown in Fig. 4(e), which is in general agreement with previous studies on laser cladding [16, 38–41]. In contrast to the clear influence of the scan speed, the powder feed rates (ranging from 5.5 g/min. to 6.5 g/min.) do not show a significant trend with the cross-section, due to the large variance in the data. This may be due to unfavorable combinations of scanning speed and powder feed rate, although this requires further study. The single-track clad settings can give some indication as to whether a multilayered part will be under- or overbuilt. In contrast to the case for single-track clads, the trend of decreasing width with increasing scan speed is not as clear for the multitrack clad samples, with an R -sq of 37.23%, and P values of 0.088 for the scanning speed and 0.018 for the feed rate (Table 4). The widths remain similar across the range of evaluated parameters, which is confirmed in Fig. 4(f); the primary exception to this statement would be the E1 setting.

3.3 Rectangular/ideal layer builds and geometry effects

Studies on both the single-track and multitrack clads show that, through modifying the deposition parameters, the originally intended layer thickness is not always obtained and, consequently, must be closely monitored during builds. Higher powder feed rates combined with slower scan speeds can result in overbuilding. This is apparent from dimensional studies of the rectangular sample heights, which ranged from 8.05 mm (± 1.32) to 13.80 mm (± 0.37), as presented in Fig. 5(a). Similar observations to these have been made in prior studies [42, 43]. In terms of the rectangular builds, under all of the examined deposition conditions, the lengths and widths are similar across all of the examined settings; there is little variation in these dimensions, with a maximum error of about 1 mm.

Consequently, as might be anticipated, the most critical DED dimensional error arises in terms of the build height control. The height control can be corrected by dividing the desired dimension by the measured value, and then multiplying by the parameter:

Adjusted Parameter

$$= \frac{\text{Programmed Dimension}}{\text{Measured Dimension}} * \text{Current Parameter Used}$$

This will indicate if the settings that are being used need to be changed; if the system parameter value remains the same, then the parameter does not require any adjustments. The adjusted parameter can increase or decrease, depending on the dimensional measurements. However, this will only help improve the dimensional target accuracy, but may not necessarily impact the surface finish and/or microstructure. It has been

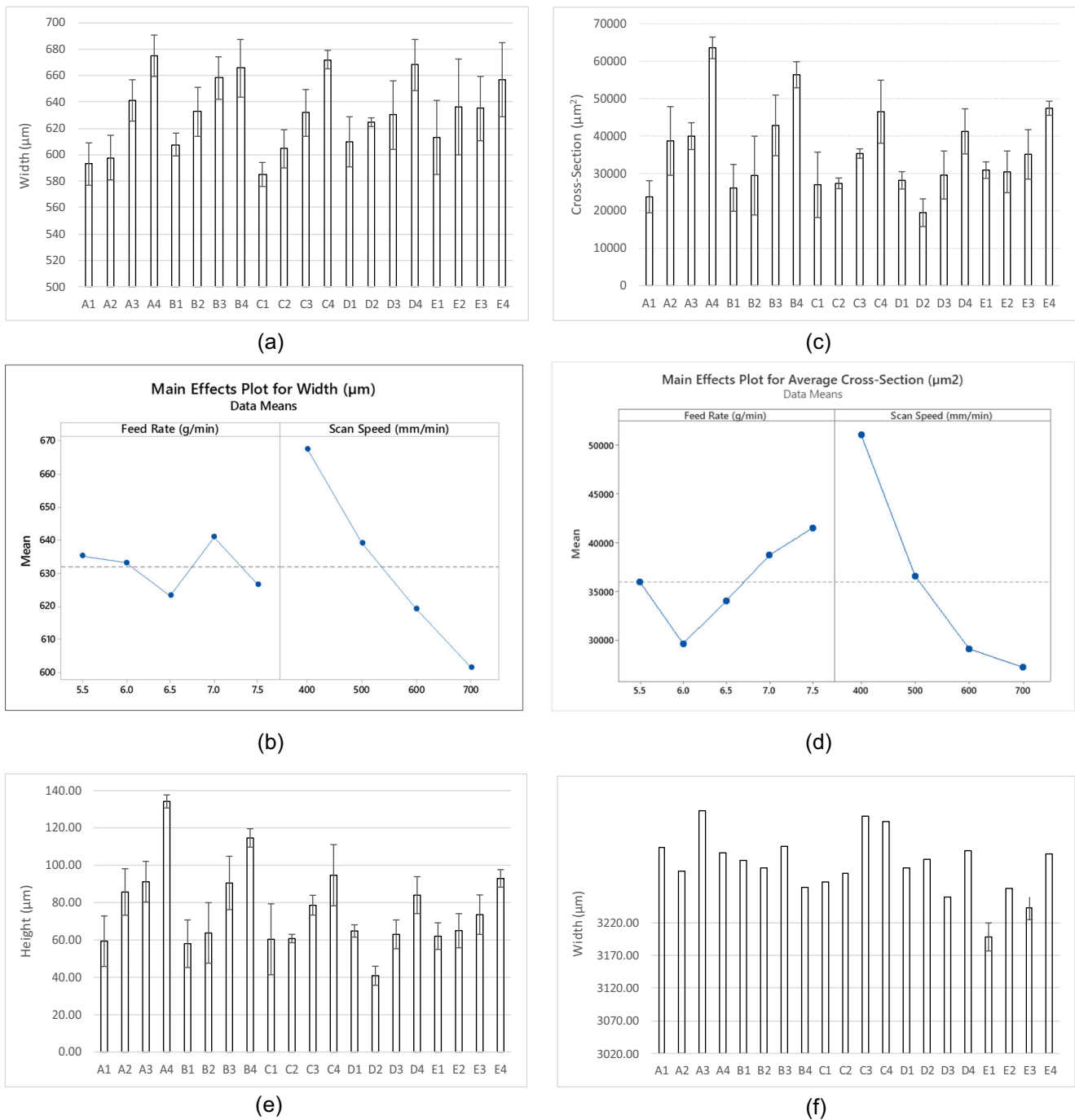
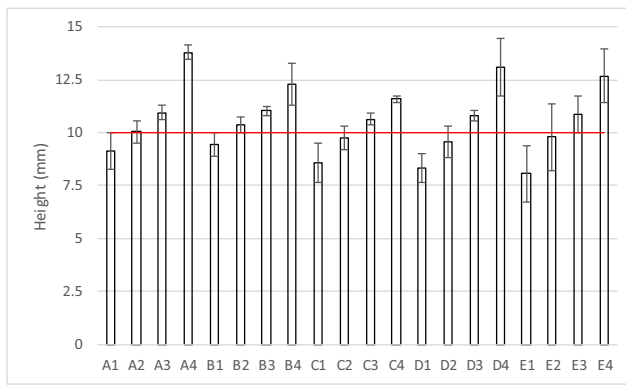


Fig. 4 **a** The effects of varying system parameters on the single-track clad widths. **b** The resultant ‘main effects plot’ for single-track clad widths. **c** The effects of varying system parameters on the single-track cross-sectional areas. **d** The resultant ‘main effects plot’ for single-track clad cross-

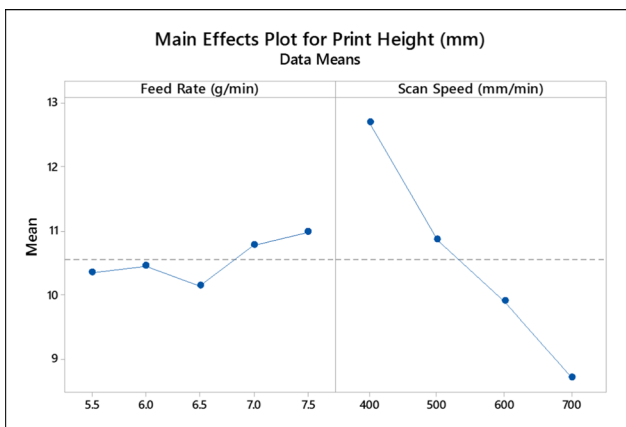
sectional areas. **e** The effects of varying system parameters on the single-track clad height. **f** Multitrack clad widths as a function of process conditions (provided previously in Table 3)

reported that the overbuilding observed with slower scan speeds is due to the higher power density, which consolidates extra powder particles [44, 45]. From the plot summarizing the primary parameter effects (Fig. 5(b)), all of the examined powder feed rates have a very similar influence, indicating the increased flexibility in selecting feed rates without impacting

the build response significantly. The major height error arises from the scanning speed, with the fastest speed underbuilding and the slowest speed overbuilding. Applying a regression to the height using the feed rate and scan speed, the determined *R*-sq value is 90.68% (Table 4). In association with this, the *P* value for the scanning speed is 0.0, highlighting the



(a)



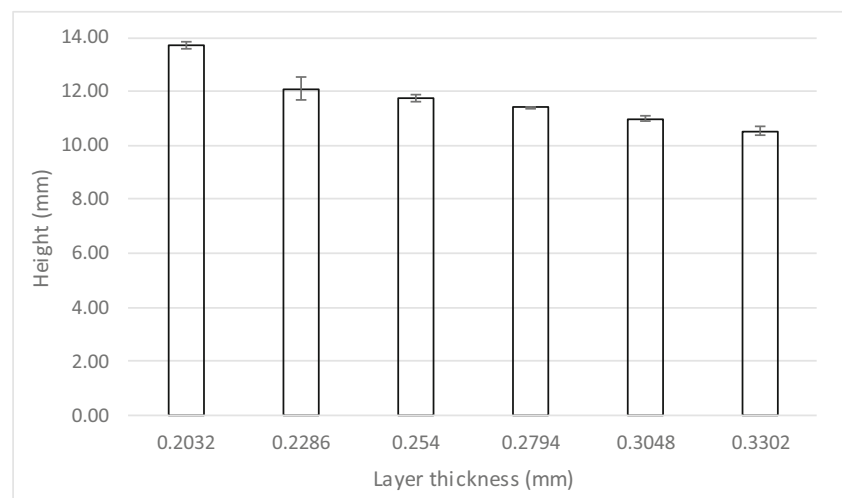
(b)

Fig. 5 **a** Geometrical measurements for the heights of the rectangular samples as a function of process parameters. The red horizontal line indicates the preprogrammed rectangle target height. **b** The composite ‘mean effects plot’ for the rectangle heights

significance of the scanning rate. In contrast, the powder feed rate has a P value of 0.062, meaning it is not as significant as the scan speed.

As noted with the rectangular builds, the component width and length are comparable across the range of examined DED

Fig. 6 Dimensional measurements for the ideal layer height samples



parameters, with the height being of more concern. To examine the effect layer thickness has on a pre-designed fixed height build in greater detail, six ‘ideal layer’ samples were also fabricated, as shown in Fig. 6. When the thickness of the deposited layer is greater than desired, it results in overbuilding. When the layer thickness is reduced, more material is consolidated, and the build rate increases, which will decrease the actual build-to-nozzle standoff distance; since the DED system cannot account for variations in the deposit height, finer layers will have a greater height error because overbuilding is more likely, and the material build “catches up” with the nozzle head. The opposite is true with a coarser layer thickness, as less material is consolidated, causing underbuilding. This is evident experimentally when the layer thickness has been changed (Fig. 6), for example from 0.2032 to 0.3302 mm. This can be related to powder defocusing, in that if the powder defocusing is below the melt pool level, the height of the deposition increases because of the increased powder concentration [31]. Powder defocusing was not a system parameter controlled in this study, but it is suggested as a possible reason for the observed results, and may warrant further study. For the present case it was apparent that it is difficult to obtain the desired layer thickness without adaptive controls to monitor the process [15, 16]. Under the A3 settings the layer thickness should have been changed to 0.3302 mm, as it was the closest to the desired height; this test would have to be conducted on each setting to find an optimal layer thickness.

In terms of build considerations with the present DED system and its operation, the rectangular samples that were initially printed have some evidence of limited surface oxidation, with subsequent prints having less. This is due to the build chamber nominally starting at atmosphere (*i.e.*, air) then, as printing continued, more Ar was used (as both the shield gas and powder carrier gas), thus reducing the extent of oxidation. Periodically there will be samples that will be more oxidized on the surface, with subsequently printed samples having a

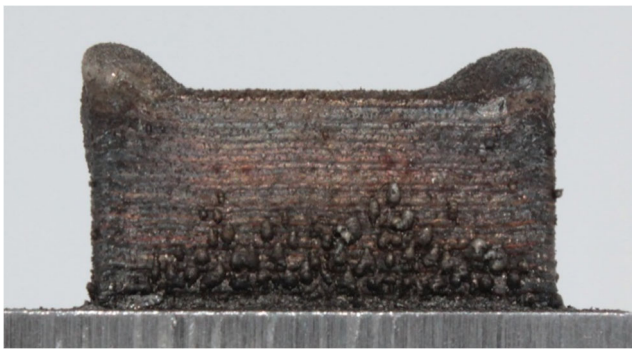


Fig. 7 Sample D4, highlighting the more extreme ‘built-up’ corner effect, due to the scanning strategy employed (the cut substrate is shown at the bottom of the image)

lower level of oxidation; this arises due to the need for periodic nozzle cleaning that requires opening the build chamber door, resulting in the chamber reverting to atmospheric conditions. There is no noticeable visual change in the single clad tracks other than the amount of oxidation. Clearly this is somewhat undesirable, with the potential to affect the inter-layer structure and bonding for multilayer builds. However, this is actually a realistic scenario for the low-cost repair of large tool steel components, as they are likely to be processed using shield gas environments rather than enclosed chambers with a controlled inert atmosphere.

All samples also contain attached powder particles, which will ultimately lead to higher ‘as-printed’ surface roughness in components, and consequently dictate the need for some limited final machining. Adhered particles were also observed on the sides of vertical surfaces. Even though particles are seen on the side and top of each of the samples, all of the examined DED conditions produced a suitable structure, except for rectangle E1; under these specific system settings, the contour continued to build but the core filling was unsuccessful. It is

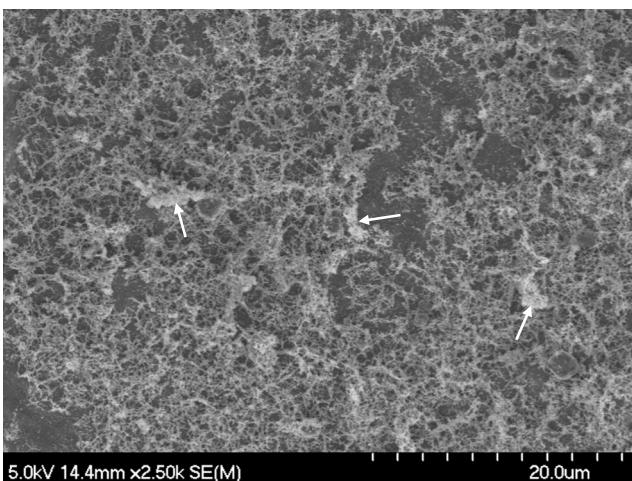
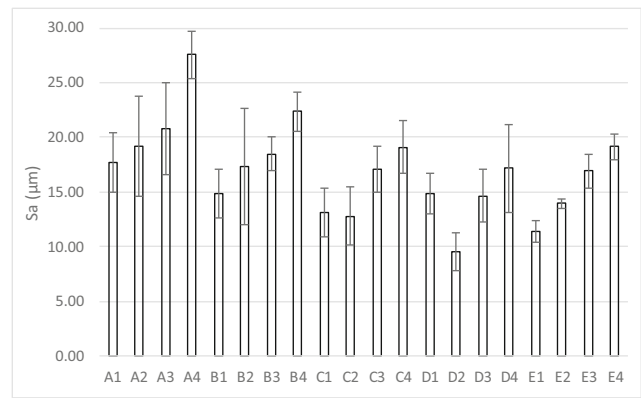
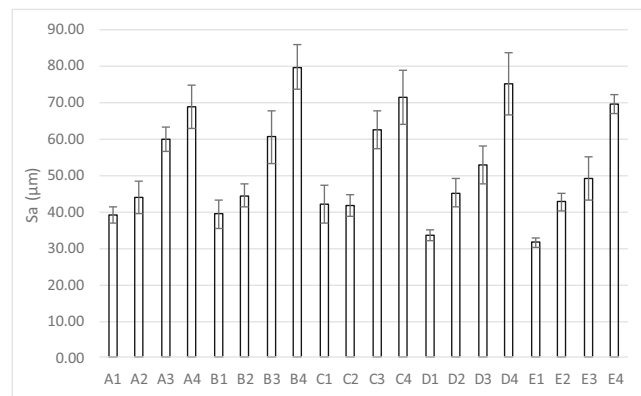


Fig. 8 Representative FE-SEM image demonstrating the formation of some limited surface oxide. Note that the oxide lightly covers the surface with a fine, fibrous morphology; some areas of higher oxide concentration are highlighted with arrows



(a)



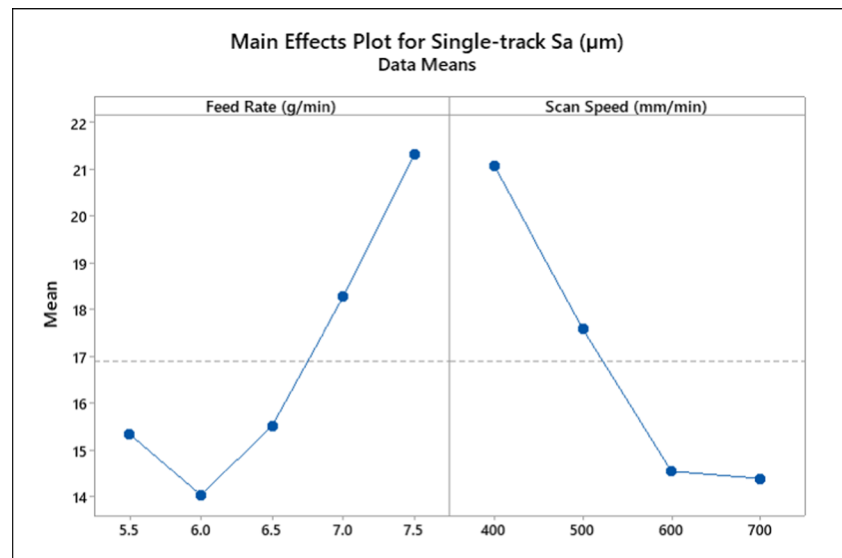
(b)

Fig. 9 Cladding surface roughness, S_a , as a function of DED process parameters (Table 3): **a** single-track and **b** multitrack clads

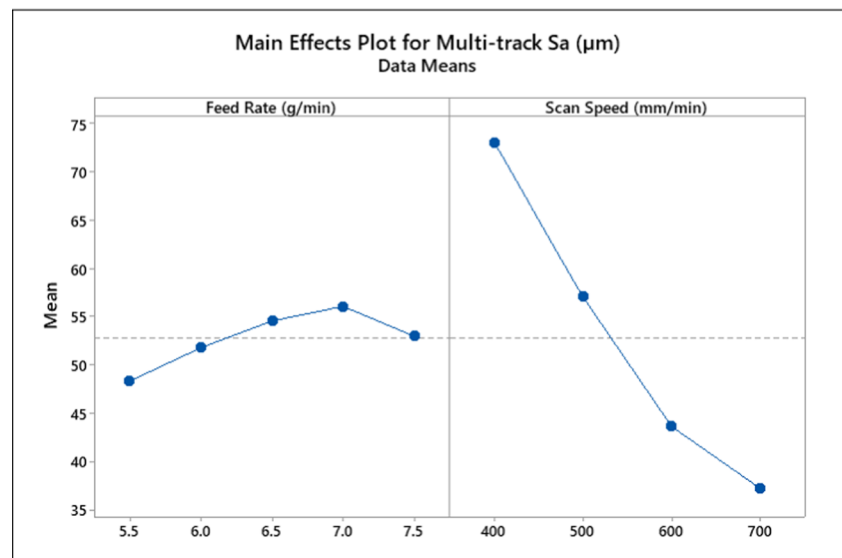
unknown why this occurred, but a reasonable hypothesis may be due to the fast-scanning speed used in combination with a low powder feed rate, resulting in under consolidation. The rectangle and ideal layer thickness samples have overbuilding on the corners, which appear to a greater or lesser extent on most of the printed samples. This was more evident in builds using the lower scanning speeds and lower feed rates, which is due to the toolpath software; as the contour is made, it will stop at the corner, pause, and proceed on toward the next corner to finish the contour. The extra pause at the corner results in more material being deposited, causing the top surface to be uneven, which is clearly demonstrated in the extreme case presented in Figure 7. The lower speeds and lower feed rates can be expected to increase this effect because the imparted energy is greater, allowing for more powder particles to be fully melted into the built structure.

A noticeable oxide layer can be seen on the sample surfaces using SEM (Fig. 8), which has a fibrous appearance. It can be envisaged that there may be entrapped oxide on powder particle regions in builds, especially if the power density is increased [46]. Since the oxide can be anticipated to be brittle, it is arguably undesirable, but any external surface oxidation would be likely removed through finish machining. In

Fig. 10 Mean effects plots of surface roughness, S_a , as a function of DED parameters for **a** the single-track clads and **b** the multitrack clads



(a)



(b)

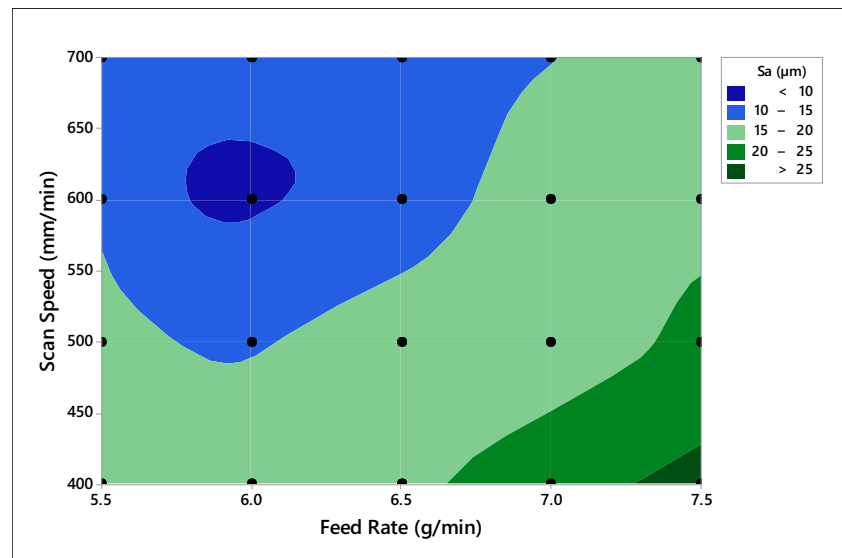
addition, this oxide ‘curtain’ makes it difficult to identify porosity on the printed surface in comparison to the porous oxide structure itself.

Table 5 System parameter significance (determined using ANOVA in Minitab®) on surface roughness values determined for the single-track and multitrack clads, and the rectangular samples

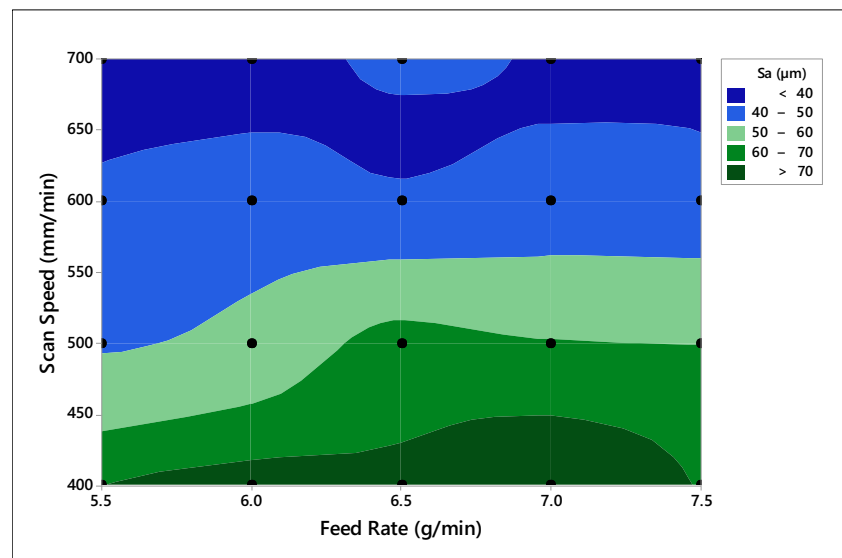
Sample	R-sq (%)	Scanning speed <i>P</i> value	Feed rate <i>P</i> value
Single-track clad	75.21	0.0	0.0
Multitrack clad	91.56	0.0	0.073
Rectangle (side)	9.75	0.235	0.577
Rectangle (top)	5.721	0.35	0.928

All the 3D samples have a distinct ‘wavy’ surface appearance, indicative of the laser DED build process. It has been previously noted that the use of inert gas atomized powders creates well-defined, individual layers when compared to water atomized powders [28]. In addition, it was shown that using gas atomized powders also resulted in more partially melted particles on the surface, leading to a higher surface roughness [28]. This is because the melt pool temperature for gas atomized powders is lower than water atomized powders, due to the increased surface coupling, arising from the powder surfaces being rougher and having more oxidation during synthesis [47]. There were no major visible signs of lack of layer fusion in the present work. In the boundary region between layers, the surface appears smooth while the side of the layer has striations that show the melt direction.

Fig. 11 Surface roughness, S_a , contour maps for **a** the single-track clads and **b** the multitrack clads



(a)



(b)

In the ideal layer samples, the larger layer thickness can be distinguished from the finest layer thickness. However, there is no significant visual change that can be seen between the differing finer layer thicknesses.

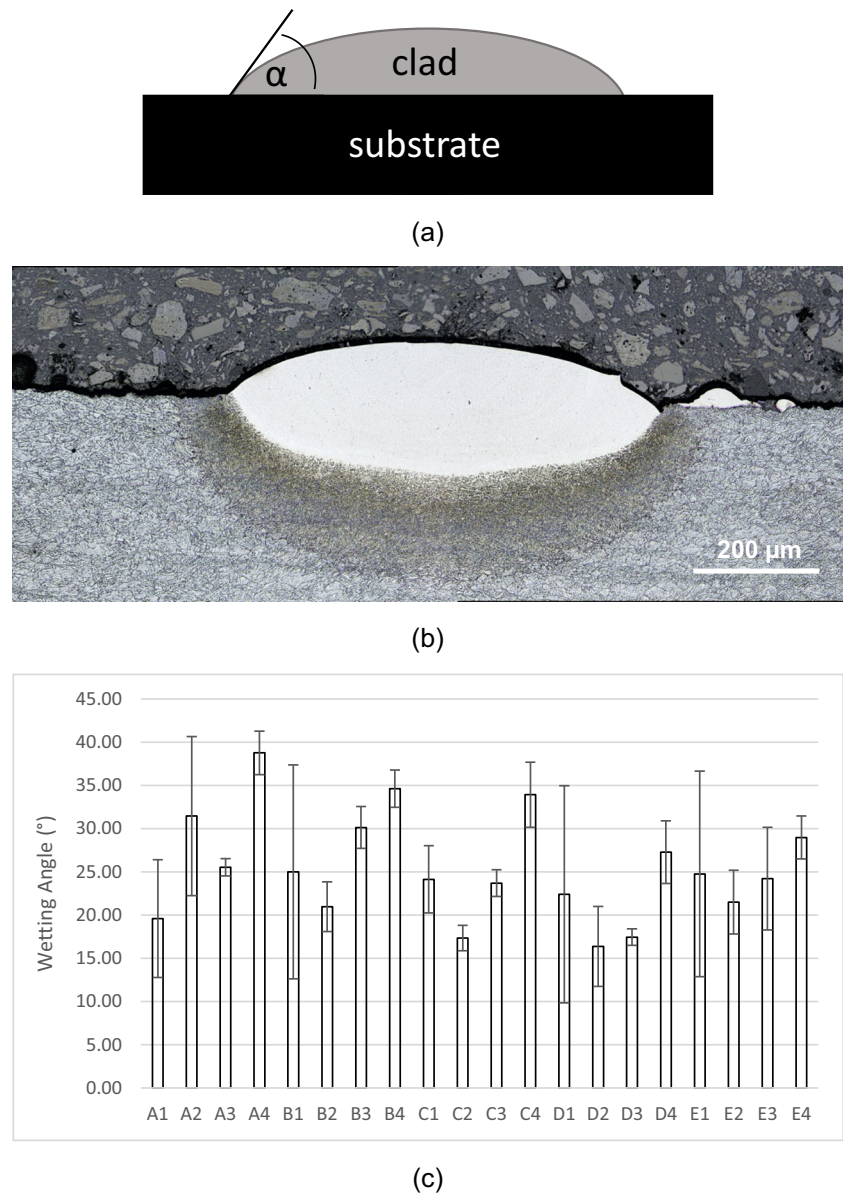
3.4 Surface roughness of single- and multitrack clads

Figure 9 summarises the mean top surface roughness measurements for the single-track and multitrack clad samples. For the case of single tracks, the surface roughness generally appeared to increase with decreasing scanning speed, with this trend clearest for parameter sets A, B, and E, and less apparent for parameter sets C and D; however, there is still a generally comparable response overall. In a similar manner, the surface

roughness for the multitrack cladding samples increases with decreasing scan speed. This was a clear trend for each of the DED parameter sets examined.

Examining the primary process variables, it is seen that the surface roughness generally increases with increasing powder feed rate for both the single- and multitrack cladding depositions (Fig. 10). However, in comparison to the influence of scan speed, for the multitrack clads the effects are more subtle, although the roughness values are much higher. As noted in the previous paragraph, the lowest surface roughness values generally occur at the highest examined scan speeds, for both the single-track and multitrack clads, which are highlighted in the ‘mean effects plots’ (Fig. 10). The multitrack clad samples follow the same trend as the single-track clads, with slower

Fig. 12 **a** The ‘wetting angle’ (α) definition used in the present work. **b** Example CLSM optical (white light) image of the cross-section of a single-track clad (processing condition B4). **c** The mean single-track clad ‘wetting angle’ as a function of laser DED process parameters

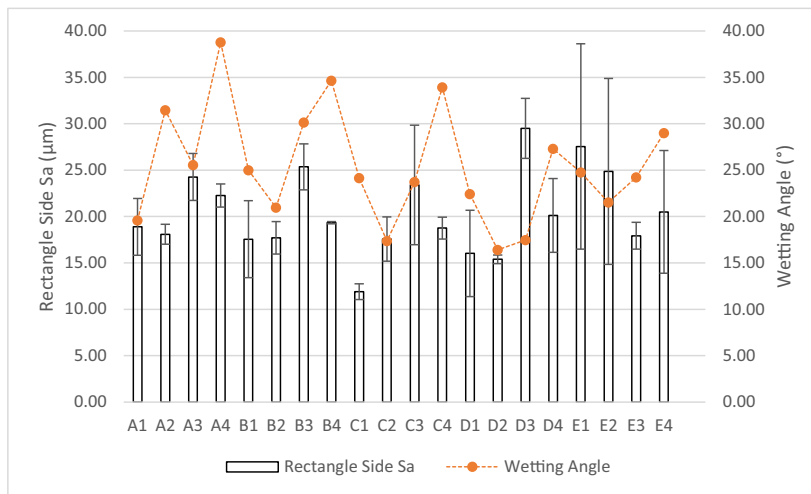


scanning speeds and higher feed rates generally producing a higher surface roughness. However, it is clear that the multi-track clad samples are significantly rougher than the single-track clads due to the waviness of the adjacent layers compared to the single-track.

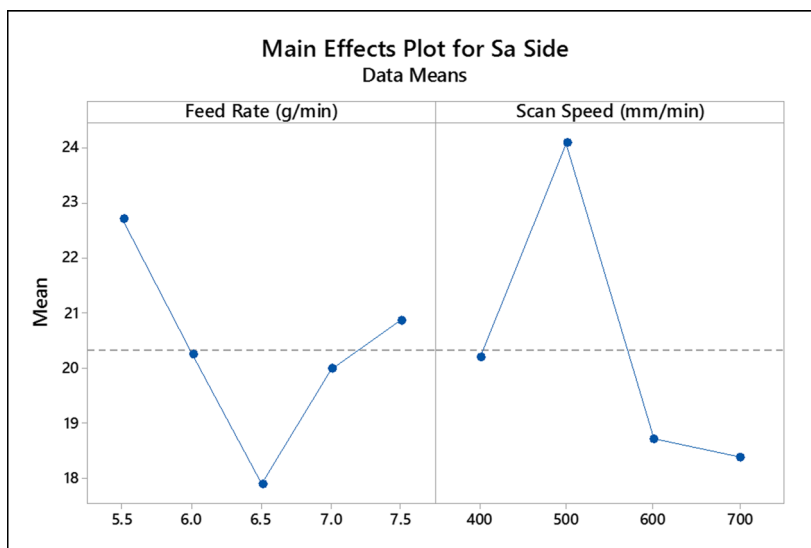
A combination of the slowest scanning speed, together with the highest feed rate, resulted in the highest surface roughness. The lower quality surface finishes (*i.e.*, higher roughness), produced by the higher feed rates, are likely due to more particles interacting with the laser beam, resulting in a smaller melt pool, as noted earlier. When the scanning speed is reduced, the surface roughness may be anticipated to decrease because there is a longer laser particle interaction period to melt the particle [23], and *vice-versa* with a faster scanning speed. The higher surface roughness for the higher feed

rates is consequently believed to arise from a greater number of partially melted particles attached to the surface. In terms of statistical analysis, the single-track clad samples have P values of 0.0 for both the feed rate and the scanning speed, and an R -sq of 75.21% (Table 5). In comparison, the multitrack clad samples have P values of 0.073 and 0.0 for the feed rate and scanning speed, respectively, and an R -sq of 91.56% (Table 5). Contour ‘maps’, relating the effects of the combined

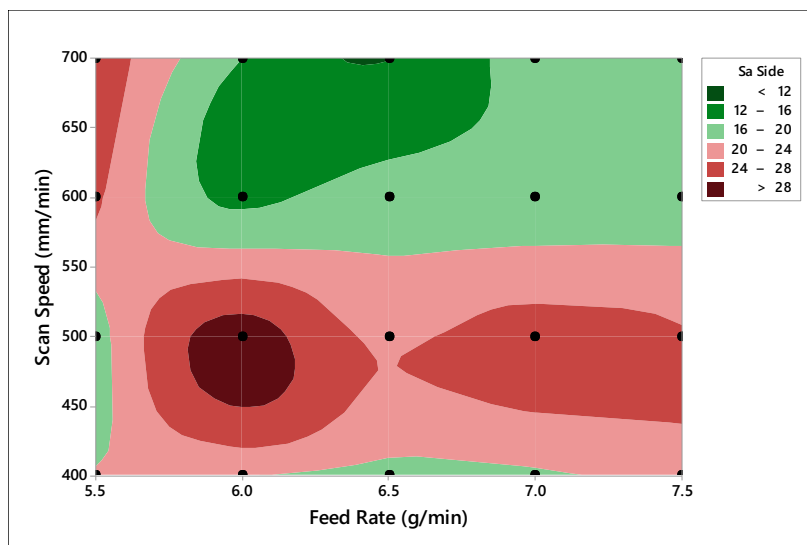
Fig. 13 **a** The mean rectangle side surface roughness, S_a , values for each of the assessed DED parameter sets; mean-value data for the wetting angles of the single-track clads (from Fig. 12) is also overlaid for comparative purposes. **b** The ‘main effects plot’ for the surface roughness of the rectangle sides. **c** The surface roughness contour map for the rectangle sides



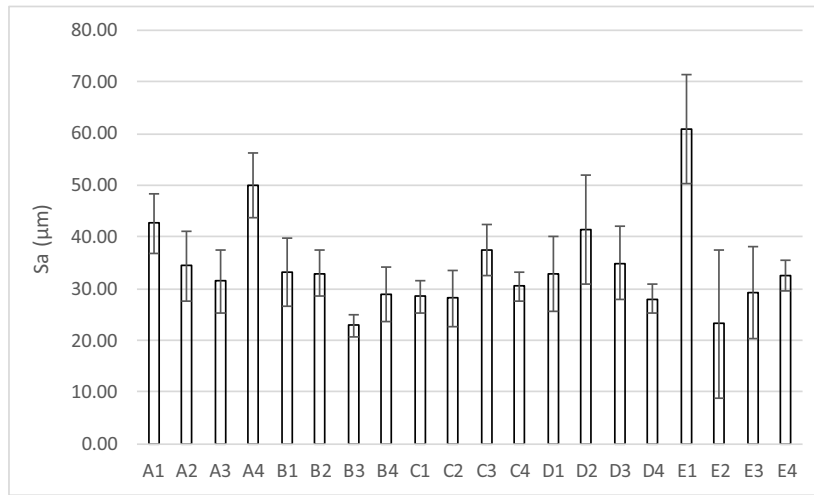
(a)



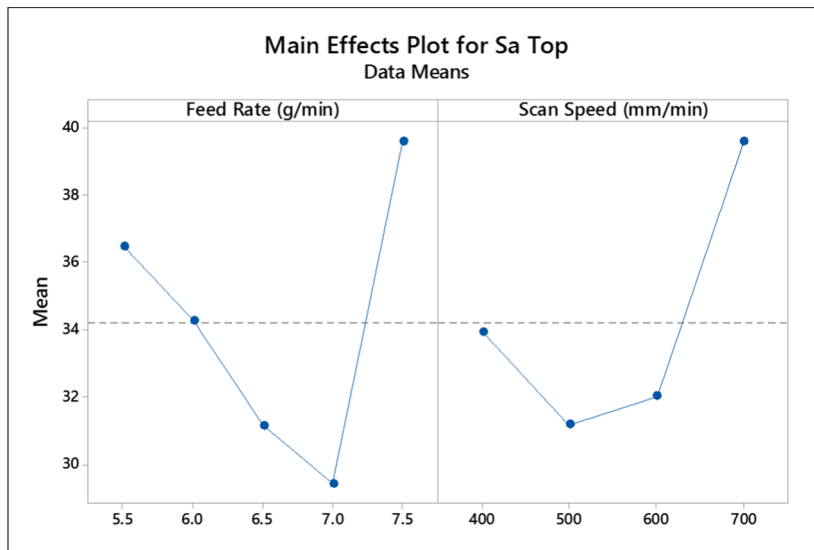
(b)



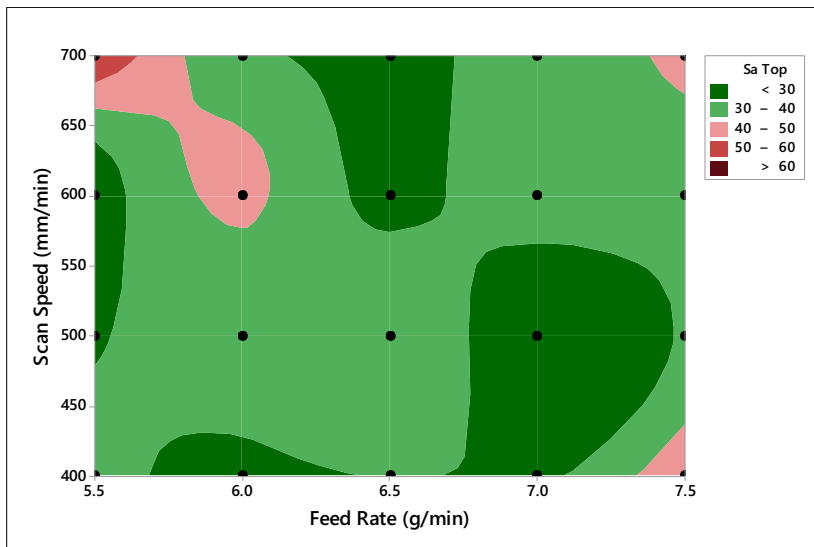
(c)



(a)



(b)



(c)

◀ **Fig. 14** **a** The mean rectangle top surface roughness, S_a , values for each of the assessed DED parameter sets. **b** The main effects plot for the surface roughness of the rectangle tops. **c** The surface roughness contour map for the rectangle tops

scanning speed and powder feed rate parameters on surface roughness, are shown for both single- and multitrack clads in Fig. 11.

To assess a nominal deposition ‘wetting angle’ for the single-track clads (defined as a ‘clad angle’, α), cross-sections (cut perpendicular to the laser scanning direction of track) were evaluated to determine the angle the clad track makes with the substrate (Fig. 12); the defined ‘wetting angle’ measurement used in the present case is shown schematically in Fig. 12(a). It is apparent that faster laser scanning speeds generate a lower angle in the single-track clads when compared to slower speeds (Fig. 12(b)). This is likely due to the melt pool flattening out due to the shorter dwell time of the laser for the faster scanning speeds. With a slower scanning speed, the temperature gradient and surface tension in the melt pool is reduced due to the higher energy input, the fluid flow decreases, and this results in the bead forming a ‘hump’ shape [48, 49].

3.5 Surface roughness of rectangular geometry samples

In order to see if there is a correlation between the wetting angle of the single clad samples and the side surface roughness of rectangular samples, the side surface roughness was determined for the rectangle builds (Fig. 13). In the ‘A’ set of samples it appears that with increasing clad angle, α (data from Fig. 12), the side surface roughness also increases, the exception being setting A2, having a lower side surface roughness. The ‘B’ and ‘D’ parameters have a general correlation between the clad angle and side roughness, with settings B4

and D3 not following this trend. The ‘C’ and ‘E’ settings do not follow the trends. Overall, based on this comparison, there does not seem to be a significant correlation between the deposit clad angle and side surface roughness. In addition, the profile of the single-track clad can vary widely across the track. Faster scanning speeds had the most variance in the clad angle, with slower scanning speeds resulting in more consistent clad profiles. This interaction of using the clad angle to predict the side surface roughness could be useful, but since there are material and heat interactions with the previous layer in multilayered builds, it becomes increasingly more difficult to predict the potential impact.

Although there is a clear spread of measured surface roughness values, as a function of the examined DED process parameters, there does not appear to be a clear trend of parameter dependence in terms of the surface roughness for either the sides (Fig. 13) or tops (Fig. 14) of the rectangular samples. This is in contrast to the prior observations for the single- and multitrack clads, where the slower scan speeds had a higher surface roughness; this observation highlights the need for caution in extrapolating 3D build expectations of surface finish for multilayer samples from single- or multitrack clad analysis. Comparing these two figures, it is clear that the side finish roughness values are consistently slightly lower than those of the top surfaces. This may be due to the larger surface area for particles to remain ‘trapped’ on top of the sample with the slower scanning speeds, combined with a larger amount of material being used, as the top surface will remain at an elevated temperature creating the possibility of bonding with these extra particles. Broadly speaking, from the contour map for the rectangle side roughness, the values determined decrease with increasing scan speed (Fig. 13(c)). The lower powder flow rates also produce a slightly higher side surface roughness, although this trend is relatively subtle, but especially notable in combination with the lower scan speeds. In comparison, the top surface roughness values show no clear trend with either the laser scanning or powder flow rates.

Fig. 15 Draft angle surface roughness, S_a , of the DED processed samples. The draft angle samples were all prepared using the A3 DED process settings (*i.e.*, powder feed rate of 7.5 g/min and laser scanning speed of 500 mm/min)

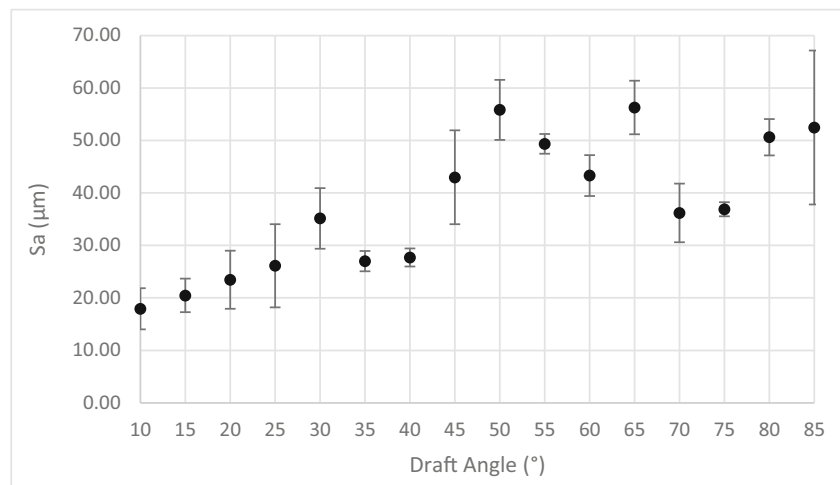
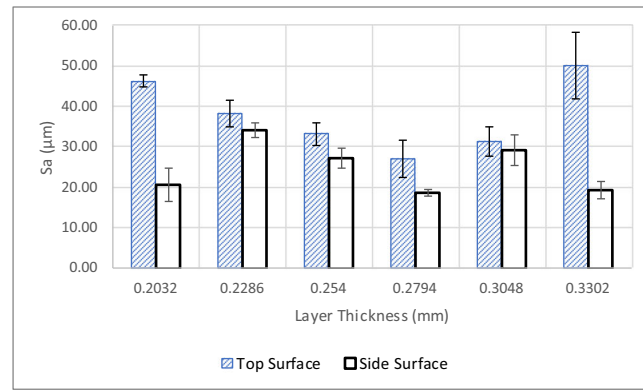
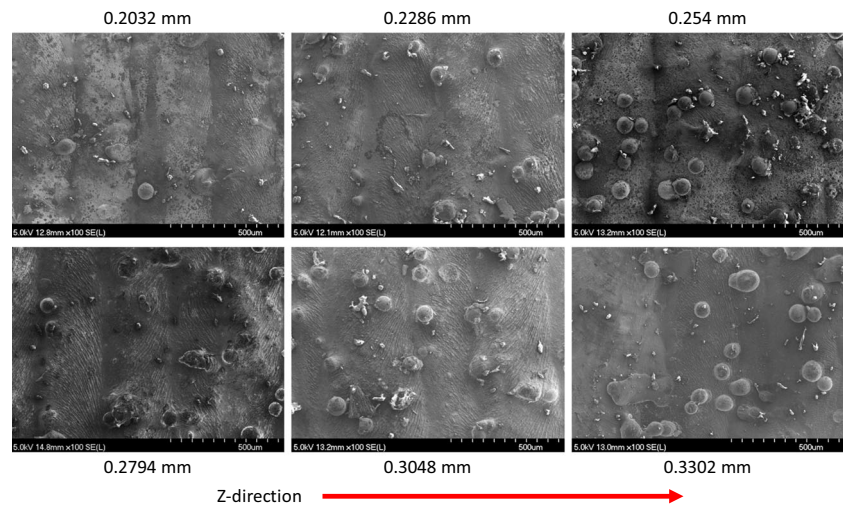


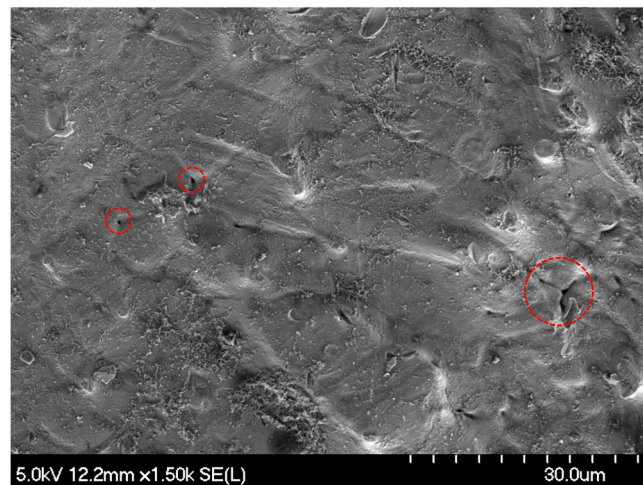
Fig. 16 **a** The mean top and side surface roughness, S_a , of the ‘ideal layer’ samples as a function of layer thickness. Samples were prepared using settings A3 from Table 3 (i.e., a feed rate of 7.5 g/min and a laser scanning rate of 500 mm/min). **b** Representative FE-SEM images of the side surfaces of the ideal layer samples shown in **a**. **c** Higher magnification FE-SEM image of the side of an ideal layer sample located between layers prepared with a layer thickness of 0.2286 mm with surface porosity highlighted by the red circles



(a)



(b)



(c)

In the literature there is conflicting evidence for the effects of the scan speed on as-printed surface roughness. Gharbi *et al.* noted that the use of higher scanning speeds and higher laser powers promoted shorter melt pool durations, which produced the best surface finishes [22]. This is attributed to

faster scanning speeds consolidating less material compared to slower speeds, thereby reducing the height of the layer, which results in a reduction of the surface ‘waviness’. The higher power contributes to improved melting of the powder particles, causing them to disperse on the surface rather than

being partially melted and agglomerating on the surface. Conversely, Mahamood *et al.* mentions that decreasing the energy density (*i.e.*, fast scanning speed) results in a higher surface roughness [23]. The rheology and production of powders can have an impact with gas atomized powders, which invariably have a higher surface roughness [50]. Under these different system parameters, the variation in surface roughness on a single DED sample can be significant, due to the attached unmelted particles on the surface. At lower powder feed rates there is less interaction with the laser beam, resulting in the laser making a more effective melt pool. The melt pool will be larger with a lower powder feed rate resulting in more melting.

Even though the varying system parameters produce different results, a clear trend in the data cannot be found. When a linear regression is performed on the surface roughness, the side *R*-sq is 9.75% and the top *R*-sq is 5.21%, indicating that there is little correlation associated with the examined the DED parameters. The *P* values for the side surface roughness are 0.577 and 0.235, for the powder feed rate and laser scanning speed, respectively. Similarly, the *P* values for the top surface roughness are 0.928 and 0.35 for the feed rate and scanning speed, respectively. It can be stated that, overall, these settings will produce very similar surface finishes. That is not to say that the settings are insufficient for building, but that clear ‘ideal’ parameter settings have not been identified. A targeted surface finish is not a sufficient measurement on its own, when selecting system parameters for 3D builds, the user must also consider the dimensions, density, and microstructure, and the resultant mechanical behavior. If a higher laser power was available, the surface roughness would likely decrease because there is more energy to fully melt the powders [15, 26]. The ‘main effects plot’ for the side surface (Fig. 13(b)), showed that changing the feed rate will impact the surface finish more than the scanning speed.

In addition, another significant parameter that helps to improve the surface finish on all sides of the rectangle samples is using a properly aligned nozzle head. If the nozzle head is slightly shifted to one side of the sample, it will deposit unintended material; when the nozzle is off-center, the powder feed nozzles spray particles on the side instead of on the subsequent layer. This will create a ‘balling’ effect on the surface, where extra material has been consolidated that continues up the sample. Evidence of this can be seen in all the samples (*e.g.*, Fig. 7), which likely increases the side surface roughness values. Due to this specific process-/equipment-related artifact, the surface roughness was not measured on the side impacted by the nozzle alignment. None of the printed surfaces would be satisfactory for most applications, and machining would still be required to achieve the required surface tolerances. In addition, for a forming mold application, designers have to account for overbuilding, so that all the original part lies inside the machining volume. By obtaining a near net shape that has a low surface roughness, the cost to

manufacture new mold tooling will decrease as less material is needed to be removed [6].

3.6 Roughness as a function of draft angle

From the data presented in Fig. 15, it is apparent that as the draft angle is increased (as previously defined in Fig. 1(b)), the ‘draft face’ surface roughness simultaneously increases. Consequently, the lower draft angles, from 10 to 45°, produce the best ‘as-deposited’ surface finish. The reduction in roughness for the shallow draft angles is likely due to the next layer being slightly offset from the previous one, which allows greater flattening out compared to when the layers are stacked normal to each other, resulting in a more pronounced individual layer at the higher draft angles. When the draft angle reaches 50°, the roughness values reach those of the top surfaces of the rectangle samples. When building a vertical structure, a small draft angle may be selected to improve the side surface roughness for a 3-axis system. This would be limited to the geometry of the desired part, but it could be incorporated in the design of vertical sides. In line with this, it has been noted in prior work that as the sloped angle increases (*i.e.*, increasing draft angle), so does the roughness of the deposited material [18, 19]. For the present case, the *P* value of the regression is 0.0, with an *R*-sq of 62.23% (Table 5), indicating that the draft angle does have a significant impact on the surface roughness.

3.7 Fabrication of ideal layer thickness test samples

Depending on the system parameters, the deposited layer can potentially be smaller or larger than the desired layer thickness. With a smaller layer thickness there should, in principle, be a finer gap between consecutive layers when compared a larger layer thickness, but this does not appear to be the case. The ‘as-deposited’ side surface finish, in terms of roughness, has been shown to be broadly consistent for the different defined layer thicknesses, assuming the scan speed and powder feed rate are the same (Fig. 16(a)). Layer thicknesses of 0.2032 mm, 0.2794 mm or 0.3302 mm were seen to produce the lowest surface roughness ($S_a \sim 20 \mu\text{m}$) on the side, although this surface does not present any clear trend within the analyzed data. The observed ‘waviness’ of a finer layer thickness is greater than with a coarser layer thickness (Fig. 16(b, c)). The surface roughness actually has a minimum with a layer thickness of 0.2794 mm, for both the top and side of the sample; in this instance the top surface roughness increases with either an increasing or decreasing layer thickness from this value. Under the A3 settings a 0.2794 mm layer thickness produces the best surface finish. The *P* values for layer thickness effects on the side and top surface roughness values are 0.626 and 0.939, respectively. Similarly, the *R*-sq value for the

side surface roughness is 6.49%, while it is 0.17% for the top surface roughness.

4 Conclusions

Based on the presented work, with the DED system employed, an optimal combination of the laser scanning and powder feed rates can be found to minimize the surface roughness. However, these settings do not show significant outliers within the range of parameters that were examined, highlighting a degree of process flexibility. Even though the tests were not always statistically significant, the results show a qualitative understanding of what is occurring. Slower scanning speeds (400 mm/min) resulted in overbuilding in the z-direction, with the opposite being true for increasing scanning speeds (700 mm/min). Ideally, the selected system settings should provide components with good dimensional accuracy and low surface roughness. Within the currently examined parameters, a recommended combination of settings for a 3D part is in the middle of the ranges examined, which would be parameter set B2, with a scanning speed of 600 mm/min and powder feed rate of 7 g/min; these conditions resulted in a top surface roughness of 32.91 μm and a side surface roughness of 17.69 μm . Slight overbuilding would be acceptable because it is likely consolidated parts will require final machining prior to use. With those considerations in mind, the B2 settings only overbuilt by 3.6% and still present an acceptable as-printed surface. Another way of improving the side surface roughness would be adding a shallow draft angle (10–25°) to a vertical wall.

The as-printed surfaces invariably have attached powder particles, which proved unavoidable within the examined range of conditions, and which clearly lead to higher surface roughness values. In the single-track and multi-track clad samples there is a clear trend of increasing surface roughness with decreasing scanning speed, with the scanning speed being more significant (P value = 0.0) in both sets than the feed rate. Printing in an air atmosphere, even with the use of a shield gas, resulted in the initial printed samples exhibiting traces of oxidation, which decreased through the build cycle. Finally, changing the layer thickness using A3 settings did not have a clear impact on the top surface roughness (P value = 0.939) and side surface roughness (P value = 0.626).

Acknowledgements The authors would also like to thank the technical support staff at QMC, Mr. François Bérubé and Mr. Pierrick Cyrenne, for assistance with setting up the DED system and printing the samples. This work was supported through the NSERC Strategic Project Network Grant Holistic Innovation in Additive Manufacturing (HI-AM) through Grant No. NETGP 494158-16.

Author contribution Mr. Owen Craig conducted all of the material characterization and data analysis work within this manuscript under the guidance of his supervisor (Prof. Plucknett); Dr. Alexandre Bois-Brochu conducted the laser DED work at QMC with his team; and Dr. Kevin Plucknett conceived the initial research plan, modified the plan where necessary, and also reviewed and edited the final manuscript.

Availability of data and material All related data can be made available upon request to the authors.

Code availability Not applicable.

Declarations

Ethics approval Not applicable. This work does not include experimentation on humans or animals.

Consent to participate Not applicable.

Consent for publication This article has been reviewed and cleared for publication by the HI-AM research committee. This includes a review by industrial partners.

Competing interests The authors declare that they have no competing interests.

References

1. ASM (1990) Properties and selection: irons, steels, and high-performance alloys, vol 1. ASM International
2. Roberts G, Krauss G, Kennedy R (1998) Tool steels, 5th edn. ASM International, Materials Park, OH
3. Smith WF (1981) Structure and properties of engineering alloys, 1st edn. McGraw-Hill Inc., New York
4. Jhavar S, Paul CP, Jain NK (2013) Causes of failure and repairing options for dies and molds: a review. Eng Fail Anal 34:519–535. <https://doi.org/10.1016/j.engfailanal.2013.09.006>
5. Taylor P, Birger EM, Moskvitin GV, Polyakov AN, Arkhipov VE (2011) Industrial laser cladding : current state and future. Weld Int 3(25):234–243. <https://doi.org/10.1080/09507116.2010.540880>
6. Gibson I, Rosen D, Stucker B (2015) Additive manufacturing technologies, 2nd edn. Springer
7. Gu D (2015) Laser additive manufacturing (AM): classification, processing philosophy, and metallurgical mechanisms
8. Zeng Z et al (January, 2020) Wire and arc additive manufacturing of a Ni-rich NiTi shape memory alloy: microstructure and mechanical properties. Addit Manuf 32. <https://doi.org/10.1016/j.addma.2020.101051>
9. Rodrigues TA et al (March, 2020) In-situ strengthening of a high strength low alloy steel during wire and arc additive manufacturing (WAAM). Addit Manuf 34. <https://doi.org/10.1016/j.addma.2020.101200>
10. Tuominen J (2009) “Engineering coatings by laser cladding—the study of wear and corrosion properties, Ph.D Dissertation,” Tampere
11. Lopes JG, Machado CM, Duarte VR, Rodrigues TA, Santos TG, Oliveira JP (2020) Effect of milling parameters on HSLA steel parts produced by wire and arc additive manufacturing (WAAM). J Manuf Process 59(October):739–749. <https://doi.org/10.1016/j.jmapro.2020.10.007>

12. Miedzinski M (2017) Materials for additive manufacturing by direct energy deposition. Chalmers University of Technology
13. Laura Cordova TT, Campos M (2017) “Powder characterization and optimization for additive manufacturing,” 56th Annu. Conf. Metall., p. 926872
14. ASTM F3187 (2016), “Standard guide for directed energy deposition of metals,” ASTM Stand., pp. 1–22. doi: 10.1520/F3187.
15. Shim DS, Baek GY, Seo JS, Shin GY, Kim KP, Lee KY (2016) Effect of layer thickness setting on deposition characteristics in direct energy deposition (DED) process. *Opt Laser Technol* 86: 69–78. <https://doi.org/10.1016/j.optlastec.2016.07.001>
16. Saboori A, Tusacciu S, Busatto M, Lai M, Biamino S, Fino P, Lombardi M (2018) Production of single tracks of Ti-6Al-4V by directed energy deposition to determine the layer thickness for multilayer deposition. *J Vis Exp* 2018(133):1–10. <https://doi.org/10.3791/56966>
17. Campbell RI, Martorelli M, Lee HS (2002) Surface roughness visualisation for rapid prototyping models. *CAD Comput Aided Des* 34(10):717–725. [https://doi.org/10.1016/S0010-4485\(01\)00201-9](https://doi.org/10.1016/S0010-4485(01)00201-9)
18. Rombouts M, Maes G, Hendrix W, Delarbre E, Motmans F (2013) Surface finish after laser metal deposition. *Phys Procedia* 41:810–814. <https://doi.org/10.1016/j.phpro.2013.03.152>
19. Wang D, Mai S, Xiao D, Yang Y (2016) Surface quality of the curved overhanging structure manufactured from 316-L stainless steel by SLM. *Int J Adv Manuf Technol* 86(1–4):781–792. <https://doi.org/10.1007/s00170-015-8216-6>
20. Adam GAO, Zimmer D (2014) Design for additive manufacturing—element transitions and aggregated structures. *CIRP J Manuf Sci Technol* 7(1):20–28. <https://doi.org/10.1016/j.cirpj.2013.10.001>
21. Mahamood RM, Akinlabi ET, Shukla M, Pityana S (2013) Characterizing the effect of laser power density on microstructure, microhardness, and surface finish of laser deposited titanium alloy. *J Manuf Sci Eng Trans ASME* 135(6):2013–2016. <https://doi.org/10.1115/1.4025737>
22. Gharbi M, Peyre P, Gorny C, Carin M, Morville S, le Masson P, Carron D, Fabbro R (2013) Influence of various process conditions on surface finishes induced by the direct metal deposition laser technique on a Ti-6Al-4V alloy. *J Mater Process Technol* 213(5): 791–800. <https://doi.org/10.1016/j.jmatprotec.2012.11.015>
23. Mahamood RM, Akinlabi ET (2017) Scanning speed and powder flow rate influence on the properties of laser metal deposition of titanium alloy. *Int J Adv Manuf Technol* 91(5–8):2419–2426. <https://doi.org/10.1007/s00170-016-9954-9>
24. Mahamood RM, Akinlabi ET (2018) Effect of powder flow rate on surface finish in laser additive manufacturing process. *IOP Conf Ser Mater Sci Eng* 391(1). <https://doi.org/10.1088/1757-899X/391/1/012005>
25. Peyre P, Gharbi M, Gorny C, Carin M, Morville S, Carron D, le Masson P, Malot T, Fabbro R (2012) Surface finish issues after direct metal deposition. *Mater Sci Forum* 706–709:228–233. <https://doi.org/10.4028/www.scientific.net/MSF.706-709.228>
26. Mahamood RM, Akinlabi ET (2014) Effect of laser power on surface finish during laser metal deposition process. *Lect Notes Eng Comput Sci* 2:965–969
27. Spierings AB, Herres N, Levy G (2011) Influence of the particle size distribution on surface quality and mechanical properties in AM steel parts. *Rapid Prototyp J* 17(3):195–202. <https://doi.org/10.1108/135525411111124770>
28. Pinkerton AJ, Li L (2003) Effects of powder geometry and composition in coaxial laser deposition of 316L steel for rapid prototyping. *CIRP Ann - Manuf Technol* 52(1):181–184. [https://doi.org/10.1016/S0007-8506\(07\)60560-5](https://doi.org/10.1016/S0007-8506(07)60560-5)
29. Alrbaey K, Wimpenny D, Tosi R, Manning W, Moroz A (2014) “On optimization of surface roughness of selective laser melted stainless steel parts: a statistical study,” *J Mater Eng Perform* 23(6):2139–2148. <https://doi.org/10.1007/s11665-014-0993-9>
30. Alfieri V, Argenio P, Caiazzo F, Sergi V (2017) Reduction of surface roughness by means of laser processing over additive manufacturing metal parts. *Materials (Basel)* 10(1). <https://doi.org/10.3390/ma10010030>
31. Zhu G, Li D, Zhang A, Pi G, Tang Y (2012) The influence of laser and powder defocusing characteristics on the surface quality in laser direct metal deposition. *Opt Laser Technol* 44(2):349–356. <https://doi.org/10.1016/j.optlastec.2011.07.013>
32. Aver'yanova IO, Bogomolov DY, Poroshin VV (2017) ISO 25178 standard for three-dimensional parametric assessment of surface texture. *Russ Eng Res* 37(6):513–516. <https://doi.org/10.3103/S1068798X17060053>
33. Hutchings I, Shipway P (2017) *Tribology: friction and wear of engineering materials*, 2nd edn
34. Barbara Illowsky SD (2013) *Introductory statistics*. OpenStax, Rice University, Houston
35. Markusson L (2017) *Powder characterization for additive manufacturing processes*. Luleå University of Technology
36. Kong RJSCY, Carroll PA, Brown P (2007) “The effect of average powder particle size on deposition efficiency, deposit height and surface roughness in the direct metal laser deposition process,” in 14th International Conference on Joining Materials, [Online]. Available: <https://www.twi-global.com/technical-knowledge/published-papers/the-effect-of-average-powder-particle-size-on-deposition-efficiency-deposit-height-and-surface-roughness-in-the-direct-metal-las>
37. Oliveira JP, Santos TG, Miranda RM (2020) Revisiting fundamental welding concepts to improve additive manufacturing: from theory to practice. *Prog Mater Sci* 107:100590. <https://doi.org/10.1016/j.pmatsci.2019.100590>
38. Caiazzo F, Alfieri V (2018) Laser-aided directed energy deposition of steel powder over flat surfaces and edges. *Materials (Basel)* 11(3). <https://doi.org/10.3390/ma11030435>
39. Caiazzo F, Alfieri V, Argenio P, Sergi V (2017) Additive manufacturing by means of laser-aided directed metal deposition of 2024 aluminium powder: Investigation and optimization. *Adv Mech Eng* 9(8):1–12. <https://doi.org/10.1177/1687814017714982>
40. Jang JH, Joo BD, Mun SM, Sung MY, Moon YH (2011) Application of direct laser melting to restore damaged steel dies. *Met Mater Int* 17(1):167–174. <https://doi.org/10.1007/s12540-011-0223-z>
41. Lee EM, Shin GY, Yoon HS, Shim DS (2017) Study of the effects of process parameters on deposited single track of M4 powder based direct energy deposition. *J Mech Sci Technol* 31(7):3411–3418. <https://doi.org/10.1007/s12206-017-0239-5>
42. Choi J, Chang Y (2005) Characteristics of laser aided direct metal/material deposition process for tool steel. *Int J Mach Tools Manuf* 45(4–5):597–607. <https://doi.org/10.1016/j.ijmactools.2004.08.014>
43. Zhong C, Biermann T, Gasser A, Poprawe R (2015) Experimental study of effects of main process parameters on porosity, track geometry, deposition rate, and powder efficiency for high deposition rate laser metal deposition. *J Laser Appl* 27(4):042003. <https://doi.org/10.2351/1.4923335>
44. Park JS, Park JH, Lee MG, Sung JH, Cha KJ, Kim DH (2016) Effect of energy input on the characteristic of AISI H13 and D2 tool steels deposited by a directed energy deposition process. *Metall Mater Trans A Phys Metall Mater Sci* 47(5):2529–2535. <https://doi.org/10.1007/s11661-016-3427-5>
45. Kobryn PA, Moore EH, Semiutin SL (2000) Effect of laser power and traverse speed on microstructure, porosity, and build height in laser-deposited Ti-6Al-4V. *Scr Mater* 43(4):299–305. [https://doi.org/10.1016/S1359-6462\(00\)00408-5](https://doi.org/10.1016/S1359-6462(00)00408-5)
46. Marya M, Singh V, Hascoet JY, Marya S (2018) A metallurgical investigation of the direct energy deposition surface repair of

- ferrous alloys. *J Mater Eng Perform* 27(2):813–824. <https://doi.org/10.1007/s11665-017-3117-5>
47. Pinkerton AJ, Li L (2005) Multiple-layer laser deposition of steel components using gas- and water-atomised powders: the differences and the mechanisms leading to them. *Appl Surf Sci* 247(1–4):175–181. <https://doi.org/10.1016/j.apsusc.2005.01.083>
48. Nam S, Cho H, Kim C, Kim Y-M (2018) Effect of process parameters on deposition properties of functionally graded STS 316/Fe manufactured by laser direct metal deposition. *Metals (Basel)* 8(8):607. <https://doi.org/10.1099/0022-1317-77-11-2819>
49. Qi H, Mazumder J, Ki H (2006) Numerical simulation of heat transfer and fluid flow in coaxial laser cladding process for direct metal deposition. *J Appl Phys* 100(2). <https://doi.org/10.1063/1.2209807>
50. Pinkerton AJ, Li L (2003) Rapid prototyping using direct laser deposition—the effect of powder atomization type and flowrate. *Proc Inst Mech Eng Part B J Eng Manuf* 217(6):741–752. <https://doi.org/10.1243/09544050360673134>

Publisher's note Springer Nature remains neutral with regard to jurisdictional claims in published maps and institutional affiliations.